Collective and local excitations in Ba_2CoTeO_6: A composite system of a spin-1/2 triangular-lattice Heisenberg antiferromagnet and a honeycomb-lattice $J_1 - J_2$ Ising antiferromagnet

Purintorn Chanlert,[1] Nobuyuki Kurita,[1] Hidekazu Tanaka,[1,*] Motoi Kimata,[2] and Hiroyuki Nojiri[2]
[1]*Department of Physics, Tokyo Institute of Technology, Meguro-ku, Tokyo 152-8551, Japan*
[2]*Institute for Materials Research, Tohoku University, Aoba-ku, Sendai 980-8577, Japan*
(Received 30 June 2017; published 15 August 2017)

We report the results of multifrequency high-magnetic-field electron-spin resonance (ESR) measurements on the highly frustrated antiferromagnet Ba_2CoTeO_6. This compound is magnetically composed of two subsystems A and B, which are described as a spin-1/2 triangular-lattice Heisenberg antiferromagnet and a honeycomb-lattice J_1-J_2 Ising antiferromagnet, respectively. Ba_2CoTeO_6 undergoes successive magnetic phase transitions at $T_{N1} = 12.0$ K and $T_{N2} = 3.0$ K. For a magnetic field H parallel to the c axis, subsystem B exhibits successive metamagnetic transitions with magnetization plateaus at one-third and one-half of the saturation magnetization. Below T_{N2}, we observed collective ESR modes for $H \parallel c$, which are characteristic of a triangular-lattice Heisenberg antiferromagnet with weak easy-plane anisotropy. We also observed a local excitation mode, which can be assigned as a single flip of the Ising-like spin of subsystem B. From a detailed analysis of the collective and local ESR modes, combined with the magnetization process, we determined the magnetic parameters of subsystems A and B, and confirmed that the two subsystems are almost decoupled.

DOI: 10.1103/PhysRevB.96.064419

I. INTRODUCTION

Frustrated magnets have been attracting considerable attention from the viewpoints of their remarkable quantum and many-body effects, which provide a spin liquid [1,2], quantized magnetization [3–5], and other phenomena. Spin frustration is classified into geometrical frustration and bond frustration. The geometrical frustration arises from the lattice geometry. Typical examples include antiferromagnets on a triangular lattice or kagome lattice. The bond frustration arises from competing exchange interactions. Square-lattice and honeycomb-lattice magnets with the antiferromagnetic nearest-neighbor J_1 and next-nearest-neighbor J_2 exchange interactions are typical examples exhibiting bond frustration.

Ba_2CoTeO_6 is a unique antiferromagnet composed of two different frustrated subsystems, a spin-1/2 triangular-lattice Heisenberg antiferromagnet (TLHAF) and a honeycomb-lattice J_1-J_2 Ising antiferromagnet (J_1-J_2 HLIAF) [6]. Ba_2CoTeO_6 crystallizes in a trigonal structure with the space group $P\bar{3}m$ [7]. There are two divalent cobalt sites, $Co^{2+}(1)$ and $Co^{2+}(2)$, with different octahedral environments. As shown in Fig. 1(a), $Co^{2+}(1)$ ions form a uniform triangular lattice in the ab plane, which is referred to as subsystem A in this paper. Subsystem A is approximately described as a spin-1/2 TLHAF [6] because the octahedral environment of $Co^{2+}(1)$ is close to a cubic environment, as observed in $Ba_3CoSb_2O_9$ [8], and the magnetic moment of Co^{2+} below liquid nitrogen temperatures is expressed by an effective spin-1/2 [9,10].

On the other hand, $Co^{2+}(2)$ ions form a bilayer triangular lattice, as also shown in Fig. 1(a), which is referred to as subsystem B. It is considered that the dominant superexchange interactions are the antiferromagnetic interlayer exchange interaction J_1 and the nearest-neighbor exchange interaction J_2 in the triangular lattice, which arise via TeO_6 octahedra that are linked with $Co(2)O_6$ octahedra by sharing corners [6,11,12]. Owing to the strong trigonal crystalline field acting on $Co^{2+}(2)$, the exchange interaction between effective spins of $Co^{2+}(2)$ ions becomes strongly anisotropic and is approximately expressed by an Ising model [6]. Because the lattice points of subsystem B are equivalent to those of a honeycomb lattice when viewed along the c axis, as shown in Fig. 1(b), subsystem B is approximately described by a J_1-J_2 HLIAF.

In our previous paper [6], we reported the results of specific heat and magnetization measurements of Ba_2CoTeO_6 using single crystals. It was found that the total magnetization is approximately given by the superposition of magnetizations for isolated subsystems A and B, which shows that subsystems A and B are approximately decoupled. Ba_2CoTeO_6 undergoes successive magnetic phase transitions at $T_{N1} = 12.0$ and $T_{N2} = 3.0$ K, which can be assigned as the spin orderings of subsystems B and A, respectively [6]. From the results of neutron-diffraction measurement on Ba_2CoTeO_6 powder performed at $T = 4.5$ K by Ivanov *et al.* [7], it was deduced that Ising-like spins of subsystem B are ordered along the c axis with the magnetic unit cell enlarged to $2a \times a$ in the ab plane, as shown in Fig. 2(a). This antiferromagnetic structure of subsystem B is stable when $J_1 < 4J_2$ [6]. For $H \parallel c$, the Ising-like subsystem B undergoes three-step metamagnetic transitions at $H_{c1}^{\parallel} = 12.3$ T, $H_{c2}^{\parallel} = 14.8$ T, and $H_s^{\parallel} = 39.0$ T with magnetization plateaus at zero, one-third, and one-half of the saturation magnetization, respectively. This magnetization process can be understood within the framework of a J_1-J_2 HLIAF. Figure 2 shows the spin structures at the magnetization plateau states, which were derived from the J_1-J_2 HLIAF model. From the analysis of the transition fields, it was found that $J_1 \simeq 2J_2$, as expected from the exchange paths [6].

The Heisenberg-like subsystem A exhibits a magnetization plateau at one-third of the saturation magnetization for $H \perp c$ owing to the quantum order by disorder [13–22]. The 1/3-magnetization plateau begins at $H_{c1}^{\perp} = 11.0$ T and

*tanaka@lee.phys.titech.ac.jp

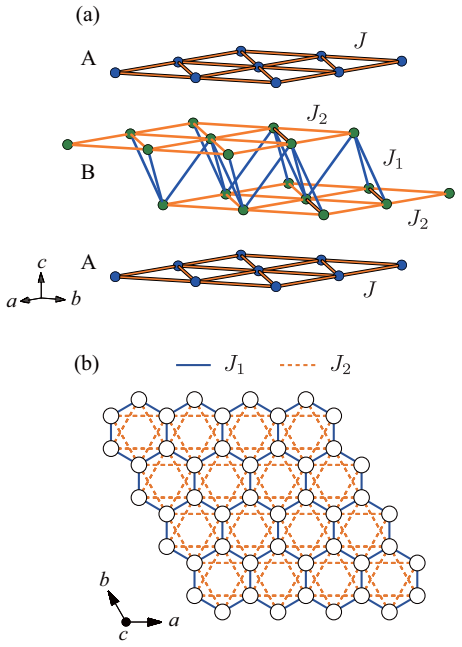

FIG. 1. (a) Magnetic subsystems A and B. Subsystem A is a uniform triangular lattice formed by Co(1) atoms. Subsystem B is composed of two uniform triangular lattices of Co(2) atoms, which are stacked with their lattice points mutually shifted to the centers of other triangles when projected onto the *ab* plane. (b) Effective magnetic model of subsystem B, which is described as a J_1-J_2 honeycomb-lattice Ising antiferromagnet.

ends at $H_{c2}^{\perp} = 18.0$ T. The magnetization of subsystem A saturates at $H_{c3}^{\perp} = 37.2$ T. The 1/3-magnetization plateau is a symbolic quantum effect in small-spin TLHAFs. The quantum fluctuation stabilizes the *up-up-down* spin state in a finite field range, which leads to the 1/3-magnetization plateau. The magnetization curve of subsystem A for $H \perp c$ is in good quantitative agreement with the theoretical result for a spin-1/2 TLHAF [17–19]. Because of the weak easy-plane anisotropy and antiferromagnetic interlayer exchange interaction, subsystem A displays no magnetization plateau for $H \parallel c$. The magnetization process of subsystem A is very similar to that observed in $Ba_3CoSb_2O_9$, which can be described as a spin-1/2 TLHAF with a uniform triangular lattice [23–28]. The entire magnetization process observed in $Ba_3CoSb_2O_9$ was quantitatively explained on the basis of a microscopic model [27,29].

In this paper, we performed multifrequency electron-spin resonance (ESR) measurements of Ba_2CoTeO_6 single crystals for $H \parallel c$ using static and pulsed high magnetic fields. We observed collective excitations of subsystem A, which are characteristic of TLHAFs with weak easy-plane anisotropy. For subsystem B, we observed local excitations characteristic of an Ising-like system and critical resonances accompanied with phase transitions at $H_{c1}^{\parallel} = 12.3$ T and $H_{c2}^{\parallel} = 14.8$ T. The observed collective and local ESR modes can be explained consistently within the magnetic models of subsystems A and B, respectively. These results confirm that subsystems A and B are almost decoupled. From the analyses of resonance data, we evaluated the magnetic parameters of both subsystems.

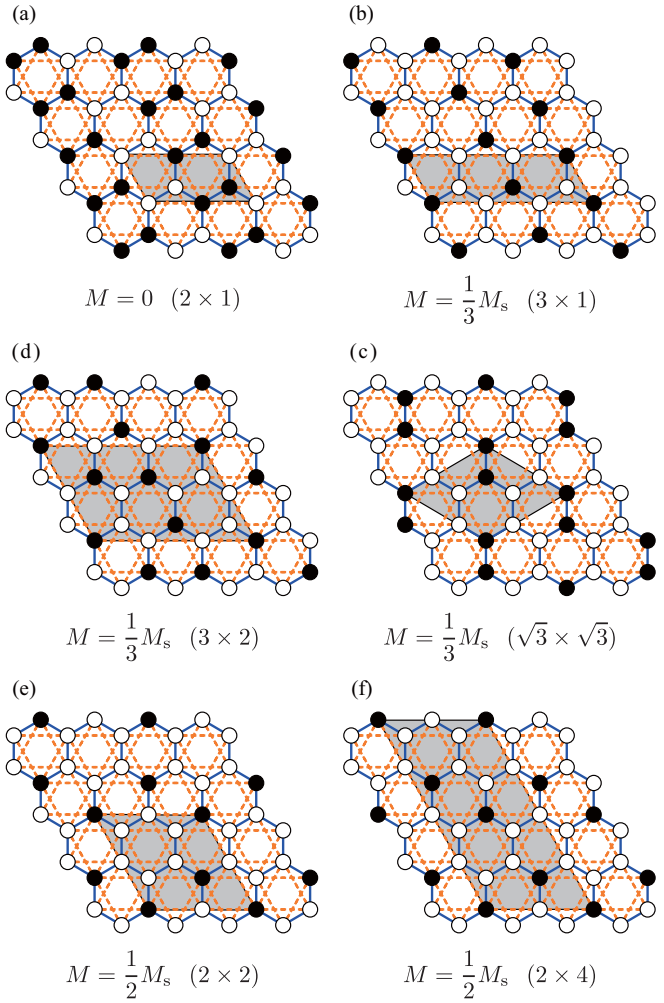

FIG. 2. Spin structures at magnetization plateau states for subsystem B [6]. Open and closed circles denote up- and down-spins, respectively. Shaded parallelograms are magnetic unit cells. Panel (a) is the 2×1 structure (AF II) observed at zero magnetic field [7]. Panels (b), (c), and (d) are candidate structures for the 1/3-plateau state, whereas panels (e) and (f) are those for the 1/2-plateau state.

II. EXPERIMENTAL DETAILS

Single crystals of Ba_2CoTeO_6 were grown by the flux method using $BaCl_2$ as the flux. The details of the preparation were reported in our previous paper [6]. Several pieces of plate-shaped single crystals with a size of approximately $3 \times 3 \times 0.3$ mm^3 were used in this experiment. The wide plane of the crystals was the crystallographic *ab* plane.

Multifrequency high-magnetic field ESR measurements in both pulsed and static magnetic fields with fixed frequencies ranging from 80 to 450 GHz were performed in the temperature range of 1.5–40 K at the Institute for Materials Research, Tohoku University. Pulsed magnetic fields up to 25 T and static magnetic fields up to 18 T were applied using a multilayer pulse magnet and a superconducting magnet, respectively. Magnetic fields were applied parallel to the *c* axis. Gunn oscillators and backward-traveling-wave tubes were used as light sources.

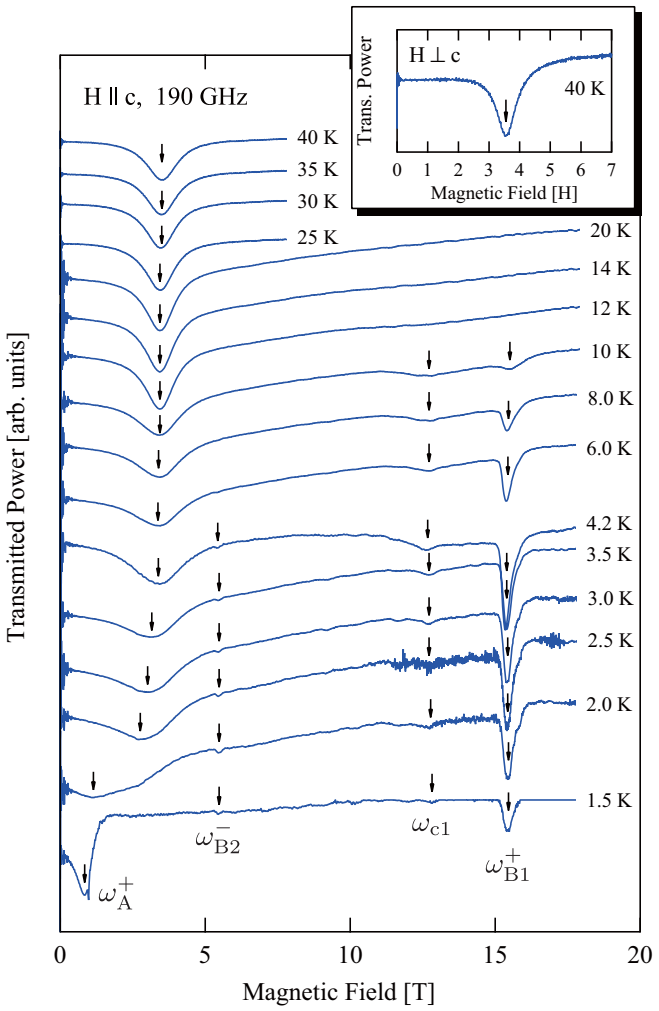

FIG. 3. Temperature evolution of electron paramagnetic resonance (EPR) and ESR spectra measured at 190 GHz for $H \parallel c$ using pulsed magnetic fields. Arrows indicate resonance fields. The data are arbitrarily shifted in the longitudinal direction for clarity. The descriptions of four resonance modes labeled $\omega_{\rm A}^{+}$, $\omega_{\rm B2}^{-}$, $\omega_{\rm c1}$, and $\omega_{\rm B1}^{+}$ are given in the text. The inset shows the EPR spectrum for $H \perp c$ measured at 40 K.

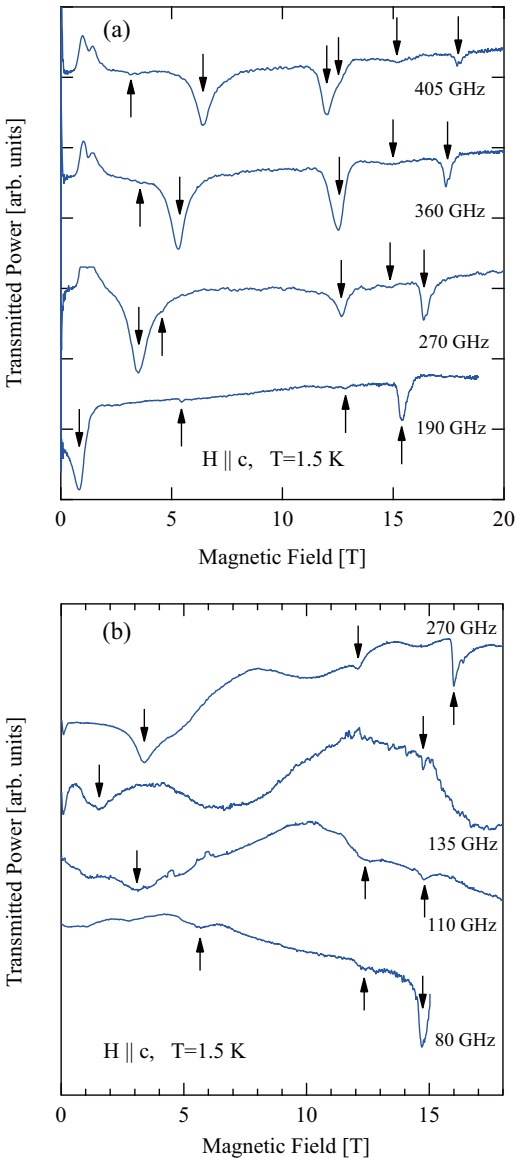

FIG. 4. Examples of ESR spectra of Ba_2CoTeO_6 measured at several frequencies for $H \parallel c$ using (a) pulsed magnetic fields and (b) static magnetic fields. Resonance data were collected at 1.5 K ($<T_{\rm N2}$). Arrows indicate resonance fields. The data are arbitrarily shifted in the longitudinal direction for clarity.

III. RESULTS AND DISCUSSION

Figure 3 shows the temperature evolution of electron paramagnetic resonance (EPR) and ESR spectra measured at 190 GHz for $H \parallel c$ using pulsed magnetic fields. At 40 K, a single resonance peak with a linewidth of approximately 1 T is observed. The EPR spectrum measured at 40 K for $H \perp c$ is shown in the inset of Fig. 3. The resonance fields of EPR for both field directions are almost the same. This indicates that the EPR signal originates from the Heisenberg-like subsystem A. From the resonance fields, the g factors of subsystem A are estimated to be $g_{\rm A}^{\parallel} = 3.88$ and $g_{\rm A}^{\perp} = 3.83$ for $H \parallel c$ and $H \perp c$, respectively. These g factors are almost the same as those observed in $Ba_3CoSb_2O_9$ [25].

As the temperature is decreased below $T_{\rm N1} = 12.0$ K, two peaks appear at $H = 12.5$ and 15.5 T. The resonance signal centered at 15.5 T is strong down to 1.5 K. An additional weak peak appears at $H = 5.5$ T below 6 K. The strong resonance peak that corresponds to EPR above $T_{\rm N1}$ starts to shift to the low-field side at $T = 3.5$ K, which is slightly above $T_{\rm N2} = 3.0$ K, and its resonance field decreases to 0.82 T at 1.5 K.

Figures 4(a) and 4(b) show examples of ESR spectra measured at several frequencies for $H \parallel c$ using pulsed and static magnetic fields, respectively. These spectra were measured at 1.5 K, which is sufficiently lower than $T_{\rm N2} = 3.0$ K. Absorption signals observed upon sweeping the field both up and down were determined as intrinsic resonance signals, which are indicated by arrows in Fig. 4. The resonance data are summarized in Fig. 5.

Six types of resonance modes are observed. Below 8 T, two strong ESR modes that consist of two branches labeled $\omega_{\rm A}^{+}$ and $\omega_{\rm A}^{-}$ are observed. At zero magnetic field, these two modes

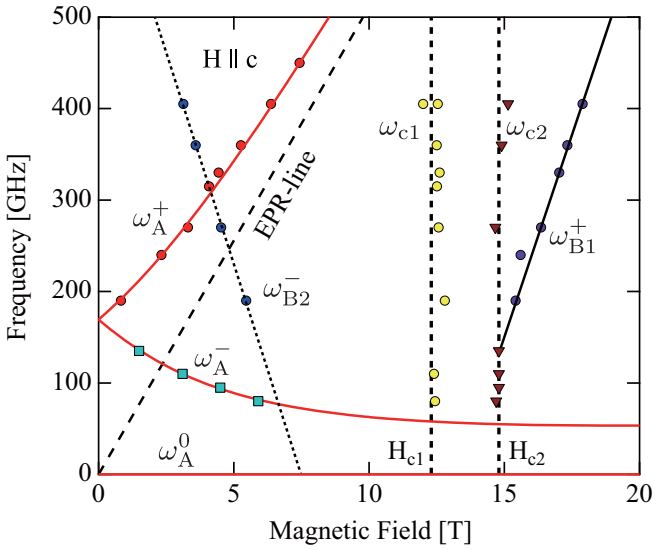

FIG. 5. Frequency-field diagram of the ESR modes in Ba_2CoTeO_6 for $H \parallel c$. Symbols denote the resonance points obtained at 1.5 K. ω_A^+ and ω_A^- are the collective ESR modes of subsystem A. The red solid curves are fits with Eq. (2) based on a six-sublattice model (see text). The red horizontal line is the ω_A^0 mode with zero frequency. The dashed line is the EPR line with $g = 3.65$, which is obtained by fitting to the $\omega_A^\pm$ mode with Eq. (2). The linear ω_{B1}^+ mode is a single flip of the up-spin of subsystem B. The black solid line is the fit by Eq. (3). The resonance modes observed at the transition fields H_{c1} and H_{c2} are the critical resonance modes for subsystem B. The weak linear ω_{B2}^- mode is an unknown mode. The thin dotted line is a linear fit to the ω_{B2}^- mode.

appear to be degenerate with an energy gap of approximately 170 GHz. As the magnetic field increases, the energy of the ω_A^+ mode increases and tends to approach the EPR line with $g = 3.88$, whereas the energy of the ω_A^- mode decreases monotonically toward zero. Because these two modes are continuously connected to the EPR mode above T_{N1}, they are assigned as the collective excitations in subsystem A. The field evolutions of the ω_A^+ and ω_A^- modes are characteristic of the collective excitations in a triangular-lattice antiferromagnet with easy-plane anisotropy rather than easy-axis anisotropy [30–32].

Two frequency-independent resonance modes (ω_{c1} and ω_{c2}) are observed at $H = 12.5$ and 14.8 T. Because these two resonance fields are almost the same as the transition fields of $H_{c1}^\parallel = 12.3$ T and $H_{c2}^\parallel = 14.8$ T for subsystem B [6], these modes are assigned as the critical resonance modes. There are two linear ESR modes labeled ω_{B1}^+ and ω_{B2}^-, which are observed for $H > H_{c2}^\parallel$ and $H < H_{c1}^\parallel$, respectively. The intensity of the ω_{B1}^+ mode is strong. Because ω_{B1}^+ and ω_{B2}^- appear below T_{N1} and their frequencies are linear in the magnetic field, which is characteristic of the resonance in an Ising-like spin system, these two modes originate from subsystem B. As shown in Fig. 3, the resonance field of the EPR, which is continuously connected to the collective ω_A^+ mode for subsystem A, is not affected by the phase transition of subsystem B at $T_{N1} = 12$ K, and the resonance fields of the ω_{B2}^-, ω_{c1}, and ω_{B1}^+ modes do not change across $T_{N2} = 3.0$ K. This result indicates that subsystems A and B are almost decoupled.

We first analyze the collective ESR modes ω_A^+ and ω_A^-, assuming that the triangular layers in subsystem A are weakly coupled by the effective interlayer exchange interaction J'. We assume that the effective interlayer exchange interaction J' is antiferromagnetic. If the interlayer exchange interaction is ferromagnetic, it does not affect the collective ESR modes, because two spins coupled by J' belong to the same sublattice. On the basis of these assumptions, we describe the magnetic model of subsystem A for $H \parallel c$ as

$$\mathcal{H}_A = \sum_{\langle i,j \rangle} \left[J \boldsymbol{S}_i \cdot \boldsymbol{S}_j + \Delta J \left(S_i^x S_j^x + S_i^y S_j^y \right) \right] + \sum_{\langle l,m \rangle} J' \boldsymbol{S}_l \cdot \boldsymbol{S}_m - \sum_i g_A^\parallel \mu_B S_i^z H, \quad (1)$$

where J and ΔJ (>0) are the exchange interaction and easy-plane-type anisotropic exchange interaction in the layer, respectively. Here, the z axis is taken to be parallel to the c axis.

The classical ground state of the model in Eq. (1) is as follows. In one triangular layer, spins lie in the layer and form a 120° structure. Two neighboring spins along the c axis are antiparallel owing to the antiferromagnetic J'. Therefore, the spin structure is composed of six sublattices. In a finite magnetic field, all the sublattice spins are canted from the triangular layer with the same canting angle. It has been theoretically demonstrated that the dispersion relation of low-energy single magnon excitations in the vicinity of the magnetic Bragg point can be described by linear spin-wave theory [33–38]. However, in a large area of the Brillouin zone, the excitation energy is significantly renormalized downward by quantum fluctuations. The ESR excitations correspond to the excitations at the magnetic Bragg point. Because the dispersion relations of single magnon excitations obtained from linear spin-wave theory are equivalent to the solutions of the classical equations of motion for sublattice spins, we calculate the resonance conditions of the collective ESR modes by solving the torque equations. In accordance with the analytical procedure of Ref. [30], we solve the torque equations for the six-sublattice model and obtain the resonance conditions as

$$\hbar\omega_A^\pm = \sqrt{\left(4J' + \frac{9}{2}J + \frac{9}{2}\Delta J\right)\left\{\frac{3\Delta J}{4} + \frac{8J' + 9J + 3\Delta J}{2(4J' + 9J + 3\Delta J)^2}(g_A^\parallel \mu_B H)^2\right\}} \pm \frac{9J + 9\Delta J}{8J' + 18J + 6\Delta J} g_A^\parallel \mu_B H, \quad (2)$$

and $\hbar\omega_A^0 = 0$. In the $\omega_A^\pm$ modes, the sublattice spins $\boldsymbol{S}_1$, $\boldsymbol{S}_2$, and $\boldsymbol{S}_3$ (or $\boldsymbol{S}_4$, $\boldsymbol{S}_5$, and $\boldsymbol{S}_6$) in a triangular layer precess with a cyclic phase difference of $\Delta\theta_{ij} = \pm 2\pi/3$. Neighboring sublattice spins $\boldsymbol{S}_i$ and $\boldsymbol{S}_{i+3}$ along the c axis precess in phase. The

ω_A^0 mode is the zero mode, which corresponds to the global rotation of spins with respect to the magnetic field.

The intralayer exchange constant J was evaluated to be $J/k_B = 20.5$ K from the saturation field $H_{c3}^{\perp} = 37.2$ T for $H \perp c$ and $g_A^{\perp} = 3.83$ using the relation $g\mu_B H_s = 9J/2$ on the assumption of $\Delta J/J \ll 1$ and $J'/J \ll 1$. The magnitude of J in Ba_2CoTeO_6 is somewhat larger than $J/k_B = 18.5$ K in $Ba_3CoSb_2O_9$ [25]. In the analysis, we only fixed the value of J. We treated the g factor as an adjustable parameter because a good fit was not obtained when the g factor was fixed to $g_A^{\parallel} = 3.88$, obtained from the EPR measurement for $H \parallel c$. The red solid curves in Fig. 5 are fits obtained using Eq. (2) with $J'/k_B = 1.6$ K, $\Delta J/k_B = 0.86$ K, and $g_A^{\parallel} = 3.65$. The agreement between the experimental and theoretical results is relatively good. Because J' and ΔJ are much smaller than J, we can deduce that subsystem A closely approximates a two-dimensional $S = 1/2$ TLHAF. These magnetic parameters of Ba_2CoTeO_6 are similar to those observed for $Ba_3CoSb_2O_9$ [25]. The g factor of $g_A^{\parallel} = 3.65$ obtained from the best fit of the collective ESR modes is smaller than $g_A^{\parallel} = 3.88$ obtained from the EPR measurement. We infer that the discrepancy arises from the dynamical shift of the EPR resonance field owing to the easy-plane anisotropy ΔJ and the weak interaction between subsystems A and B. The lattice points of subsystem A are located at the centers of the hexagons of subsystem B when projected on the ab plane, as shown in Fig. 1. Because the ordering of Ising spins of subsystem B does not have hexagonal symmetry, as shown in Fig. 2(a), the effective field acting on subsystem A from subsystem B is not uniform. To analyze the weak interaction between subsystems A and B, we have to consider the 12-sublattice model for subsystem A, which is based on a $2\sqrt{3}a \times \sqrt{3}a$ enlarged magnetic unit cell.

Next we analyze the strong ω_{B1}^{+} mode observed above $H_{c2}^{\parallel} = 14.8$ T. The candidate spin structures for $H > H_{c2}^{\parallel}$ are shown in Figs. 2(e) and 2(f) [6]. Because the frequency of the ω_{B1}^{+} mode increases with increasing magnetic field, this mode is attributed to the flip of an up-spin in the Ising-like subsystem B. The energy of the flip of one up-spin is calculated as

$$\hbar\omega_{B1}^{+} = g_B^{\parallel}\mu_B H - (J_1 + 2J_2)/2, \tag{3}$$

where J_1 and J_2 are the nearest- and next-nearest-neighbor exchange interactions in subsystem B, respectively, as shown in Fig. 1. $g_B^{\parallel}$ is the g factor for $H \parallel c$ in subsystem B. This resonance condition is common to all the up-spins shown in Figs. 2(e) and 2(f). Fitting Eq. (3) to the resonance data for the ω_{B1}^{+} mode, we obtain $g_B^{\parallel} = 6.27$ and $(J_1 + 2J_2)/k_B = 112$ K. The black solid line in Fig. 5 is the fit with these parameters. Within the framework of a J_1-J_2 HLIAF, the saturation field for $H_s^{\parallel}$ is given by [6]

$$g_B^{\parallel}\mu_B H_s^{\parallel} = 3(J_1 + 2J_2)/2. \tag{4}$$

Using $g_B^{\parallel} = 6.27$ and $(J_1 + 2J_2)/k_B = 112$ K, the saturation field is calculated as $H_s^{\parallel}(\text{cal}) = 39.8$ T, which is in agreement with the experimental saturation field of $H_s^{\parallel}(\text{exp}) = 39.0$ T.

The critical fields $H_{c1}^{\parallel}$ and $H_{c2}^{\parallel}$ for $H \parallel c$ are expressed as [6]

$$g_B^{\parallel}\mu_B H_{c1}^{\parallel} = \begin{cases} 2J_2 & (\text{for } J_1 \geqslant 2J_2), \\ J_1 & (\text{for } J_1 < 2J_2), \end{cases} \tag{5}$$

and

$$g_B^{\parallel}\mu_B H_{c2}^{\parallel} = \begin{cases} (3J_1 - 2J_2)/2 & (\text{for } J_1 \geqslant 2J_2), \\ (6J_2 - J_1)/2 & (\text{for } J_1 < 2J_2). \end{cases} \tag{6}$$

Using Eq. (5), $H_{c1}^{\parallel}(\text{exp}) = 12.3$ T, and $(J_1 + 2J_2)/k_B = 112$ K, the exchange constants J_1 and J_2 are evaluated as $J_1/k_B = 60.1$ K and $J_2/k_B = 25.9$ K for $J_1 \geqslant 2J_2$ and $J_1/k_B = 51.9$ K and $J_2/k_B = 30.1$ K for $J_1 < 2J_2$. Substituting these exchange constants in Eq. (6), we obtain $H_{c2}^{\parallel}(\text{cal}) = 15.2$ T, which is consistent with the observed value of $H_{c2}^{\parallel}(\text{exp}) = 14.8$ T. These results indicate that subsystem B can be described by a J_1-J_2 HLIAF for $H \parallel c$.

The weak linear ω_{B2}^{-} mode, the frequency of which decreases with increasing magnetic field, cannot be described by the flip of one down-spin in the structure of Fig. 2(a). The origin of the ω_{B2}^{-} mode has not yet been identified.

IV. CONCLUSION

We have presented the results of multifrequency ESR measurements of Ba_2CoTeO_6 using pulsed and static high magnetic fields for $H \parallel c$. Ba_2CoTeO_6 is composed of two subsystems A and B, which are described as an $S = 1/2$ TLHAF with weak easy-plane anisotropy and a J_1-J_2 HLIAF, respectively. We observed the collective ESR excitations in subsystem A, and two critical resonances at $H_{c1}^{\parallel} = 12.3$ T and $H_{c2}^{\parallel} = 14.8$ T and local excitations in subsystem B. The collective mode of subsystem A composed of two branches is such that three sublattice spins forming a 120° structure in a triangular layer precess with a cyclic phase difference of $\pm 2\pi/3$. The strong local excitation mode of Ising-like subsystem B observed for $H > H_{c2}^{\parallel}$ can be interpreted as the single flip of an up-spin. Analyzing these ESR modes, we evaluated the exchange interaction, anisotropy, and g factor in each subsystem. Because the observed collective and local ESR modes can be explained consistently within the magnetic models of subsystems A and B, respectively, and the temperature dependences of the collective and local ESR modes are uncorrelated, we can confirm that these two subsystems are almost decoupled.

ACKNOWLEDGMENTS

This paper was supported by Grants-in-Aid for Scientific Research (A) (Grants No. 26247058 and No. 17H01142) and (C) (Grant No. 16K05414) from Japan Society for the Promotion of Science. This work was performed under the Inter-University Cooperative Research Program of the Institute for Materials Research, Tohoku University (Proposals No. 16H0022 and No. 17H0062).

[1] P. Fazekas and P. W. Anderson, Philos. Mag. **30**, 423 (1974).
[2] L. Balents, Nature (London) **464**, 199 (2010).
[3] S. Miyahara and K. Ueda, J. Phys.: Condens. Matter **15**, R327 (2003).
[4] S. Nishimoto, N. Shibata, and C. Hotta, Nat. Commun. **4**, 2287 (2013).
[5] S. Capponi, O. Derzhko, A. Honecker, A. M. Läuchli, and J. Richter, Phys. Rev. B **88**, 144416 (2013).
[6] P. Chanlert, N. Kurita, H. Tanaka, D. Goto, A. Matsuo, and K. Kindo, Phys. Rev. B **93**, 094420 (2016).
[7] S. A. Ivanov, P. Nordblad, R. Mathieu, R. Tellgren, and C. Ritter, Dalton Trans. **39**, 5490 (2010).
[8] Y. Doi, Y. Hinatsu, and K. Ohoyama, J. Phys.: Condens. Matter **16**, 8923 (2004).
[9] A. Abragam and M. H. L. Pryce, Proc. R. Soc. A **206**, 173 (1956).
[10] M. E. Lines, Phys. Rev. **131**, 546 (1963).
[11] K. Yokota, N. Kurita, and H. Tanaka, Phys. Rev. B **90**, 014403 (2014).
[12] T. Koga, N. Kurita, M. Avdeev, S. Danilkin, T. J. Sato, and H. Tanaka, Phys. Rev. B **93**, 054426 (2016).
[13] A. V. Chubukov and D. I. Golosov, J. Phys.: Condens. Matter **3**, 69 (1991).
[14] T. Nikuni and H. Shiba, J. Phys. Soc. Jpn. **62**, 3268 (1993).
[15] A. Honecker, J. Phys.: Condens. Matter **11**, 4697 (1999).
[16] J. Alicea, A. V. Chubukov, and O. A. Starykh, Phys. Rev. Lett. **102**, 137201 (2009).
[17] D. J. J. Farnell, R. Zinke, J. Schulenburg, and J. Richter, J. Phys.: Condens. Matter **21**, 406002 (2009).
[18] T. Sakai and H. Nakano, Phys. Rev. B **83**, 100405 (2011).
[19] C. Hotta, S. Nishimoto, and N. Shibata, Phys. Rev. B **87**, 115128 (2013).
[20] D. Yamamoto, G. Marmorini, and I. Danshita, Phys. Rev. Lett. **112**, 127203 (2014).
[21] D. Sellmann, X. F. Zhang, and S. Eggert, Phys. Rev. B **91**, 081104 (2015).
[22] O. A. Starykh, Rep. Prog. Phys. **78**, 052502 (2015).
[23] Y. Shirata, H. Tanaka, A. Matsuo, and K. Kindo, Phys. Rev. Lett. **108**, 057205 (2012).
[24] H. D. Zhou, C. Xu, A. M. Hallas, H. J. Silverstein, C. R. Wiebe, I. Umegaki, J. Q. Yan, T. P. Murphy, J.-H. Park, Y. Qiu, J. R. D. Copley, J. S. Gardner, and Y. Takano, Phys. Rev. Lett. **109**, 267206 (2012).
[25] T. Susuki, N. Kurita, T. Tanaka, H. Nojiri, A. Matsuo, K. Kindo, and H. Tanaka, Phys. Rev. Lett. **110**, 267201 (2013).
[26] G. Quirion, M. Lapointe-Major, M. Poirier, J. A. Quilliam, Z. L. Dun, and H. D. Zhou, Phys. Rev. B **92**, 014414 (2015).
[27] G. Koutroulakis, T. Zhou, Y. Kamiya, J. D. Thompson, H. D. Zhou, C. D. Batista, and S. E. Brown, Phys. Rev. B **91**, 024410 (2015).
[28] J. Ma, Y. Kamiya, T. Hong, H. B. Cao, G. Ehlers, W. Tian, C. D. Batista, Z. L. Dun, H. D. Zhou, and M. Matsuda, Phys. Rev. Lett. **116**, 087201 (2016).
[29] D. Yamamoto, G. Marmorini, and I. Danshita, Phys. Rev. Lett. **114**, 027201 (2015).
[30] H. Tanaka, S. Teraoka, E. Kakehashi, K. Iio, and K. Nagata, J. Phys. Soc. Jpn. **57**, 3979 (1988); **60**, 2484 (1991).
[31] W. Palme, F. Mertens, O. Born, B. Lüthi, and U. Schotte, Solid State Commun. **76**, 873 (1990).
[32] H. Tanaka, U. Schotte, and K. D. Schotte, J. Phys. Soc. Jpn. **61**, 1344 (1992).
[33] O. A. Starykh, A. V. Chubukov, and A. G. Abanov, Phys. Rev. B **74**, 180403(R) (2006).
[34] W. H. Zheng, J. O. Fjærestad, R. R. P. Singh, R. H. McKenzie, and R. Coldea, Phys. Rev. B **74**, 224420 (2006).
[35] A. L. Chernyshev and M. E. Zhitomirsky, Phys. Rev. B **79**, 144416 (2009).
[36] A. Mezio, C. N. Sposetti, L. O. Manuel, and A. E. Trumper, Europhys. Lett. **94**, 47001 (2011).
[37] M. Mourigal, W. T. Fuhrman, A. L. Chernyshev, and M. E. Zhitomirsky, Phys. Rev. B **88**, 094407 (2013).
[38] E. A. Ghioldi, A. Mezio, L. O. Manuel, R. R. P. Singh, J. Oitmaa, and A. E. Trumper, Phys. Rev. B **91**, 134423 (2015).